Measuring image resolution in Ultrasound Localization Microscopy

V. Hingot, A. Chavignon, B. Heiles, O. Couture

Measuring image resolution in Ultrasound Localization Microscopy

V. Hingot, A. Chavignon, B. Heiles, O. Couture

Abstract— The resolution of an imaging system is usually determined by the width of its point spread function and is measured using the Rayleigh criterion. For most system, it is in the order of the imaging wavelength. However, super resolution techniques such as localization microscopy in optical and ultrasound imaging can resolve features an order of magnitude finer than the wavelength. The classical description of spatial resolution no longer applies and new methods need to be developed.

In optical localization microscopy, the Fourier Ring Correlation has showed to be an effective and practical way to estimate spatial resolution for Single Molecule Localization Microscopy data. In this work, we wish to investigate how this tool can provide a direct and universal estimation of spatial resolution in Ultrasound Localization Microscopy. Moreover, we discuss the concept of spatial sampling in Ultrasound Localization Microscopy and demonstrate how the Nyquist criterion for sampling drives the spatial/temporal resolution tradeoff.

We measured spatial resolution on five different datasets over rodent's brain, kidney and tumor finding values between 11 μm and 34 μm for precision of localization between 11 μm and 15 μm. Eventually, we discuss from those in vivo datasets how the spatial resolution in Ultrasound Localization Microscopy depends on both the localization precision and the total number of detected microbubbles.

This study aims to offer a practical and theoretical framework for image resolution in Ultrasound Localization Microscopy.

Index Terms—Ultrasound Localization Microscopy, Fourier Ring Correlation, Temporal and Spatial Resolutions, Nyquist Criterion

This work was supported in part by the European Reseach Council under the European Union Horizon H2020 programme/ERC Consolidator grand agreement N° 772786-ResolveStroke.

V. Hingot is with Sorbonne Université, CNRS, INSERM, Laboratoire d'Imagerie Biomédicale, Paris, France (vincent.hingot@upmc.fr).

A. Chavignon is with Sorbonne Université, CNRS, INSERM, Laboratoire d'Imagerie Biomédicale, Paris, France (arthur.chavignon@upmc.fr).

O. Couture is with Sorbonne Université, CNRS, INSERM, Laboratoire d'Imagerie Biomédicale, Paris, France (olivier.couture@upmc.fr).

B. Heiles is with T.U Delft, Maresca Lab, Delft, Netherlands (b.heiles@tudelft.nl).

I. INTRODUCTION

THE classical definition of the resolution of an imaging system is its ability to distinguish close objects and is usually derived from the system's Point Spread Function (PSF) using the Rayleigh criterion [1]. Because of diffraction, the width of the PSF is usually limited to the order of the imaging wavelength and the resolution as defined with the Rayleigh criterion is limited to half the imaging wavelength. Localization based methods like Single Molecule Localization Microscopy (SMLM) in optics [2]–[4] and Ultrasound Localization Microscopy (ULM) in ultrasound [5]–[10], differ from conventional imaging, they rely on the subwavelength localization of individual and punctual sources. This allows a resolution improvement far beyond the PSF based resolution limits and creates a need for new methods to measure resolution.

The precision at which microbubbles (MB) could be localized was first used as an indicator of resolution. The first studies primarily compared the distribution of the localizations with the width of a tube with flowing MB to estimate this localization precision [8], [11]–[13]. Other studies proposed a maximum localization precision based on the uncertainty of time of flights using the Cramer Rao lower bound [14]. However, it was later demonstrated that the resolution of the imaging system alone was insufficient to describe the resolution of images as motion artifacts [15]–[17] and acquisition times [18], [19] were equally important in ULM.

Several methods were proposed directly on the final images, to account for image resolution in the sense of finding the smallest separable features. For instance, it was proposed to analyze features directly on images, and define the resolution using statistical considerations on a vessel profile [3] or the separability at a bifurcation [20]. Although they are technically adapted for in vivo imaging, they rely on a crucial step of selection and segmentation which in itself can introduce heavy biases which limit their application and generalization. Moreover, the vasculature is usually complex and tortuous and therefore misrepresented in 2D.

In this study, we wish to build on this previous characterization of the resolution and to provide both practical and theoretical tools to describe resolution in ULM. The first concept we want to introduce is the Fourier Ring Correlation (FRC) to measure the resolution derived from the consistency of the spatial frequency content. The second is the notion of spatial sampling and the necessity to acquire enough samples to ensure adequate coverage of the image. Indeed, localization microscopy is not a conventional imaging method but rather a digital sampling and the issues of spatial resolution are tightly associated with the Shannon/Nyquist theorem. With those two notions, we propose two approaches to spatial resolution for ULM, a practical measure based on the FRC, and a theoretical model based on both the localization precision and on a typical sampling length. This length is the Nyquist dimension and represents the quality of the spatial coverage by the detected positions of the MB.

The localization error is the average precision δ_{Loc} at which MB can be localized on the images. It depends on many factors including signal to noise ratio, efficiency of clutter filters and precision of the localization algorithms. As the dimensions of the PSF for our acquisitions is similar in both directions, we consider axial and lateral localization error to be similar and combine them in a single average error. It is an ultimate limit for the resolution.

Although it is still debated whether the refreshing rate of MB can be described as a deterministic process based on microvascular flow [18] or a probabilistic process described by a Poisson's distribution [19], [21], [22], it is consensual that a large number of samples is required to reach super resolution. This is best described with the Nyquist/Shannon sampling theorem stating that structures finer than twice the Nyquist dimension δ_{Nyq} defined in (1) can't be appropriately reconstructed [23], [24]. It is the maximum resolution obtainable when the whole vascular space is explored by MB. Seeing that a pixel is considered complete when a MB has been localized in it, we can consider that the size of a pixel, otherwise seen as the distance between two neighboring pixels, depends on the expected localized MB density ρ. Similarly to Nyquist sampling theory, we can consider that the maximum resolution attainable spatial frequency is half the normalized density $\rho^{1/\kappa}$, where $\kappa = 1,2,3$ the dimension in space. It is measured on the whole image.

$$\delta_{\mathrm{Nyq}} = \frac{2}{\rho^{1/\kappa}} \qquad (1)$$

Spatial resolution R can then be modeled as the root mean square of the localization error and the Nyquist dimension (2).

$$\mathrm{R} = \sqrt{\delta_{\mathrm{Loc}}^2 + \delta_{\mathrm{Nyq}}^2} \qquad (2)$$

Nonetheless, this definition allows for a synthetic characterization of the tradeoff between the spatial and acquisition time as the Nyquist dimension is a direct function of MB detection and therefore of the acquisition time.

A crucial question for image reconstruction is the choice of the finest grid size that allows a meaningful representation of MB localizations density map. We propose that this choice can be motivated by the calculation of both the FRC curve and the theoretical estimation of the resolution. We foresee that these considerations on the resolution could help researchers better understand their data and represent their images in richer and more relevant ways.

II. Material & Methods

A. Animal experimentation

In order to cover different imaging situations, we performed this study on five different datasets. The first dataset for ULM is the rat's brain after craniotomy BrainInfusion [18] that we chose to use here for general reference as it was already published and is available upon request. During the acquisition, MB were injected at a constant and slow rate to ensure low and steady MB concentration. For comparison, a second rat brain BrainBolus was imaged with MB injected in a unique bolus. Acquisitions were also performed over a mouse subcutaneous tumor and a rat's kidney to produce a third and fourth datasets Tumor and KidneyBolus. A fifth dataset was produced from the rat's kidney by applying motion compensations strategies KidneyMoCo.

All experimental procedures were performed in accordance with the European Community Council Directive and approved by the institutional committee C2EA-59:" Comité d'éthique en matière d'experimentation animale Paris Centre et Sud" under the protocols 2015-23 and APAFIS # 16874-2017122914243628 v9, and by the institutional committee 34 under the protocol APAFIS #25169-202008071746473.

Experimental procedures were thoroughly described in [6], [18], [20]. Animals were anesthetized and a catheter placed in the jugular vein. For the rat's brain experiments, a cranial window was carved to expose the naked brain which was immediately covered with saline and acoustic gel. For the rat's kidney, a small incision was performed on the side of the animal so as to allow the stabilization of the organ and limit respiratory motions to the minimum.

B. ULM acquisition sequence and processing

All the datasets were acquired on a Supersonic Imagine ultrafast system using a 15 MHz probe (128 elements, 0.1 mm pitch). Acquisitions sequences consist of sending a set of compounded plane waves (PW) that are then beamformed using a Delay and Sum method and saved every second. All imaging parameters are summed up in Table 1. No contrast specific sequence was used. Frame rates are given after compounding. Although they were not directly measured, the MI of these acquisition are sufficiently low to no burst MB, and should therefore be within FDA standards.

	MB Dose (µL)	Injection method	Frame rate (Hz)	Compounding	Number of frames
BrainInfusion	400	Infusion	1000	-5:5:5	240 k
BrainBolus	200	Bolus	1000	-5:5:5	182 k
Tumor	100	Bolus	500	-11:2:11	30 k
KidneyBolus	300	Bolus	1000	-5:5:5	182 k
KidneyMoCo	300	Bolus	1000	-5:5:5	182 k

Table 1: Injection and Imaging parameters for ULM in the different rodent datasets

On the beamformed data, a combination of Singular Value Decomposition (SVD) filters (removing of the 10 first singular values per bloc of 800 frames) and temporal Butterworth high pass filters (2nd order, 50 Hz cut-off) were applied to extract MB signals from surrounding tissue signal.

Individual MB were localized using a radial symmetry-based algorithm and tracked using the *simpletracker* code adapted from the Kuhn-Munkres algorithm for assignment, which was developed for single particle tracking (https://github.com/tinevez/simpletracker). MB whose track was shorter than 20 points were discarded.

KidneyMoCo is similar to KidneyBolus except that motion was compensated in a two steps frame to frame method using affine registration on tissue low pass filtered as described in [15]. For each bloc of 800 compounded frames, all the frames were registered on the central frame of the bloc. A second step consists in registering all the central reference frames to allow the adequate registration for all the frames.

All tracks were interpolated to a 1 µm distance between consecutive points and binned on 1 µm x 1 µm pixel grid as showed on Fig. 1. The evaluation of the Nyquist dimension was performed on the raw detection prior to this interpolation step.

C. Fourier Ring Correlation to measure the resolution

The FRC is a method that can be directly computed from the images, which makes it applicable to both in vitro and in vivo situations. It provides a correlation criterion on the spatial frequency content of the dataset to estimate the resolution. It was first introduced in cryo-microscopy and proved to be robust, independent of the imaging conditions and have since then become a standard method in optical nanoscopy and SMLM [25], [26]. FRC codes were adapted to ULM data from https://github.com/bionanoimaging/cellSTORM-MATLAB/.

The original list of tracks is randomly split in two form two sub-images Im_1 and Im_2. The correlation of the spatial frequency content is calculated as the normalized correlation of the two spectrum F_1 and F_2 along iso-spatial frequency rings r (3).

$$\mathrm{FRC}(r) = \frac{\sum_{\mathrm{ring}} F_1(r)F_2(r)^*}{\sqrt{\sum_{\mathrm{ring}}|F_1(r)|^2 \sum_{\mathrm{ring}}|F_2(r)|^2}} \qquad (3)$$

This creates a curve that starts at 1 for low spatial frequencies that are evenly distributed in the dataset, before decreasing and eventually tending to 0 for high spatial frequencies that do not contribute more than noise with consistent information on the final image.

To calculate the FRC curve as in (3), the list of tracks is randomly split in two as in Fig. 2(a). The random assignation is performed by taking odd and even numbered tracks. As the number of tracks is high, the randomization method does not affect the FRC method. The variation between random assignations is less than 1 μm. Then, two independent sub-images can be reconstructed from those two subsets as illustrated in Fig. 2(b). The 2D Fourier transforms of these sub-images can be calculated as in Fig. 2(c). The FRC can then be calculated as the correlation of these two Fourier transforms along iso-frequency rings corresponding to the colored circles.

The resolution can be derived from this FRC curve using various thresholding methods thus defining the resolution as the inverse of the spatial frequency where the FRC drops below the threshold. Fixed threshold at 0.5 and 1/7 have been used but more advanced methods seem to have taken their place in SMLM.

The σ threshold curve computes the maximum spatial frequency that allows a correlation higher than the noise equivalent. The bit-based curves which computes the highest spatial frequency that allows the collection of information required to fill a half bit with signal [27], [28]. Images can be decomposed into signal and noise. In the calculation of the FRC for such a decomposition is a noise correlation term which depends on the number of pixels N in the ring. Both threshold curves depend on the number of pixels within the iso frequency ring. It is common to use threshold curves proportional to these curves, and we will focus here on the and the 2σ and ½ bit threshold curves corresponding respectively to a correlation higher than twice the equivalent noise level and the information required to fill a half bit. The 2-σ (in green) and ½ bit (in red) curves are displayed on Fig. 2(d) and resolution is determined as the intersection with the FRC curve. A smoothing window of 10 points was used on the FRC curve prior to resolution determination. In case two or more crossing can be observed, we always chose the one corresponding to the lower resolution.

III. Results

A. Resolution measurements in vivo

The FRC curves are presented in Fig. 3, start at 1 for low frequencies and drop around zeros for higher frequencies. Sharper looking images have FRC curves extending further to the right, indicating that higher frequencies are present in the dataset. The measured resolutions with the 2 threshold criterions are presented in Table 2.

	FRC 2σ	FRC ½ bit	Model
BrainInfusion	9 μM	11 μM	12 μM
BrainBolus	10 μM	13 μM	14 μM
KidneyBolus	22 μM	34 μM	17 μM
KidneyMoCo	20 μM	25 μM	19 μM
Tumor	23 μM	29 μM	23 μM

An advantage of the FRC method is that it can also be extended to its directional equivalent called the Fourier Line Correlation (FLC). Instead of correlating the two spatial spectrums on iso-frequency rings, it can be integrated along a straight line orthogonal to a given wave vector as can be seen on Fig. 4(a). This operation is repeated along all wave vector of the 2D plane to reconstruct a complete FLC image representing the consistency of the frequency content in a given direction as can be seen in Fig. 4(b) with the isolines. The values of the FLC along the vertical and horizontal lines enable the measurement of the axial and lateral resolutions as for the final ULM image.

B. Localization Precision

The localization precision depends on multiple factors: primarily on the accuracy of localization algorithm [20], the efficiency of the clutter filtering [29], but also on beamforming methods [30]–[32], and can also be heavily impacted by the label density on each frame [18], [33] as it is fundamental that MB signals do not overlap.

Given that MB can be paired and tracked on sufficiently long trajectories, we postulate that the localization precision can be estimated as the average deviation of each MB along a smoothed track. This smoothed track was obtained using the smooth function from matlab which makes a sliding average on 5 points, in axial and lateral coordinates. Indeed, we can assume that the trajectories of microbubbles follow a relatively smooth and straight trajectory of the blood flow, aside in turbulent and heavily tortuous vascularization. MB tracks that were shorter than 20 points were discarded in the process.

This localization precision can be measured for all MB tracks as described in Fig. 5(a) and the distribution of errors can be represented as a violin plot as in Fig. 5(b). The localization precision is then defined as the mean of this distribution. Overall, the difference between datasets is only of a few μm and seems to be convincingly in the order of $\lambda/10$.

C. Temporal sampling and Nyquist dimension

A good spatial sampling is achieved with the acquisition of enough MB to fill the whole image with fine enough resolution.

Fig. 6(a) shows the instantaneous MB count, which should be proportional to the intravascular MB concentration along time. Fig. 6(b) displays the cumulative MB count representing the total density of sample used to calculate the Nyquist dimension. The total MB count is of several million of detections for each acquisition. For all the data acquired as boluses, the saturation curves in Fig. 6(c) show a more rapid growth but also quickly a plateau whereas the infusion has a steadier and complete filling.

The Nyquist dimension is plotted for the different datasets in Fig. 6(d). This Nyquist dimension is a direct representation of the acquisition time as it is a direct function of MB count, which is in itself a function of MB concentration and acquisition time.

It is worth noting than in all the conditions, reaching the 10 μm mark took more than a full minute while it takes longer and longer to reach for smaller Nyquist dimension. Still, reaching small Nyquist dimension does not grant a high resolution as the limiting factor is ultimately the localization precision.

D. Fundamental spatial/temporal resolution tradeoff

To explore the link between the spatial resolution and acquisition time, we can compute the resolution as measured with the FRC calculated at different time points and represent it as a function of the resolution we modeled in (2). Both the resolutions measured with the 2σ (in green) and the ½ bit (in red) thresholds are represented in Fig. 7. All the final resolutions as measured and predicted can be found in Table 2. Globally, all curves are aligned around the first diagonal, indicating an overall relevance for the modelisation, especially for the two brain datasets in Fig. 7(a) and (b), where there is no motion.

The resolution measured with the ½ bit threshold and the 2σ threshold seems to follow parallel temporal behaviors even though the 2σ is slightly but consistently smaller. In the other datasets, the predicted resolution is strongly underestimated as it does not account for motions. In the KidneyMoCo dataset in Fig. 7(c), where motions were corrected, the prediction is closer although still a little underestimated. For the tumor in Fig. 7(d), the modeled resolution is slightly underestimated.

All these examples demonstrate how the FRC and Nyquist dimension can be used in practice to measure and predict the resolution of an ULM acquisition.

IV. Discussion

The FRC curve is a simple yet effective way to measure spatial resolution in ULM. It provides a reading richer than the localization precision or individual vessel segmentation as it characterizes the final image in its globality. The FRC measure does not depend on the imaging system, nor on the operator but on the choice of the threshold. In optical nanoscopy, the question of the threshold has long been debated and is to this day still not consensual.

The first studies proposed to use fixed arbitrary thresholds at 0.5 or 0.2 although they have been shown to overestimate the resolution [27]. The σ curves and bit based methods where later introduced [27].

Nonetheless, the FRC is quite versatile and can be extended in various ways. In particular, we showed that the FLC could provide resolution estimated in all directions. It is important as ultrasound imaging is often anisotropic. The FRC can also be easily implemented in 3D by correlating along iso-frequency shells instead of rings, and is often refers to as Fourier Shell Correlation (FSC).

Moreover, FRC is not really specific to ULM. For any imaging modality that can produce two independent images or two independent realization of a media/sample, the FRC curve could be computed and should provide a resolution measurement. In particular, it could be applied to ultrafast Doppler or any imaging modality.

It is also important to keep in mind that the FRC is a tool to estimate the resolution with advantages and drawbacks, and in some conditions, it will underperform. For instance, the measurement can easily be biased for very under-sampled data or when strong and local artefacts appear. This can create spurious correlations which may under or overestimate the resolution reading. It can appear because of aliasing or quantization errors, or because of some processing effects. A good indicator of a clean measurement is to have a regular FRC curve without strong and irregular peaks.

We also introduced a synthetic model for spatial resolution that can be summarized with the localization precision and the Nyquist dimension. It describes the resolution as the error associated with the complete ULM process which is classically the root mean square of all the sources of errors. Here, we accounted for the localization error via the localization precision, and a sampling error via the Nyquist dimension, but the model could be extended to describe a motion-based error, an aberration-based error, etc…

It should be noted than a hypothesis for the Nyquist dimension is that the vasculature is considered homogeneous. If the vasculature is non-homogeneous, for instance in the kidney, where the middle of the medullar area is almost not vascularized, this can introduce an overestimation of the Nyquist dimension and therefore of the modeled resolution.

Still, this synthetic form allows for an expression of the trade-off between spatial and temporal resolution in ULM as the acquisition time is driving the Nyquist dimension.

V. Conclusion

In this study, we proposed a practical and theoretical framework for the description spatial resolution in Ultrasound Localization Microscopy. We adapted the Fourier Ring Correlation to the field of ultrasound as a simple and general tool to adapt the notion of resolution for localization microscopy data, directly on in vivo images and independently of the operator and imaging system. Because of its simplicity and versatility, we foresee that the FRC can become a valuable tool for ultrasound imaging in general as it can provide a simple measure for image resolution not only for ULM but to any imaging modality.

Moreover, the simplicity and generality of the model we introduced can serve as a base for more advanced descriptions of spatial and temporal resolution in ULM.

References

[1] « The Theory of Sound | book by Rayleigh | Britannica ». https://www.britannica.com/topic/The-Theory-of-Sound (consulté le juin 22, 2020).

[2] E. Betzig *et al.*, « Imaging Intracellular Fluorescent Proteins at Nanometer Resolution », *Science*, vol. 313, nº 5793, p. 1642-1645, sept. 2006, doi: 10.1126/science.1127344.

[3] S. T. Hess, T. P. K. Girirajan, et M. D. Mason, « Ultra-High Resolution Imaging by Fluorescence Photoactivation Localization Microscopy », *Biophys. J.*, vol. 91, nº 11, p. 4258-4272, déc. 2006, doi: 10.1529/biophysj.106.091116.

[4] M. J. Rust, M. Bates, et X. Zhuang, « Sub-diffraction-limit imaging by stochastic optical reconstruction microscopy (STORM) », *Nat. Methods*, vol. 3, nº 10, p. 793-796, oct. 2006, doi: 10.1038/nmeth929.

[5] C. Errico *et al.*, « Ultrafast ultrasound localization microscopy for deep super-resolution vascular imaging », *Nature*, vol. 527, nº 7579, p. 499-502, nov. 2015, doi: 10.1038/nature16066.

[6] O. Couture, V. Hingot, B. Heiles, P. Muleki-Seya, et M. Tanter, « Ultrasound Localization Microscopy and Super-Resolution: A State of the Art », *IEEE Trans. Ultrason. Ferroelectr. Freq. Control*, vol. 65, nº 8, p. 1304-1320, août 2018, doi: 10.1109/TUFFC.2018.2850811.

[7] K. M. Christensen-Jeffries, « Super-resolution ultrasound imaging with microbubbles », PhD Thesis, King's College London, 2017.

[8] M. A. O'Reilly et K. Hynynen, « A super-resolution ultrasound method for brain vascular mapping », *Med. Phys.*, vol. 40, nº 11, nov. 2013, doi: 10.1118/1.4823762.

[9] K. Christensen-Jeffries, R. J. Browning, M.-X. Tang, C. Dunsby, et R. J. Eckersley, « In vivo acoustic super-resolution and super-resolved velocity mapping using microbubbles », *IEEE Trans. Med. Imaging*, vol. 34, nº 2, p. 433–440, 2015.

[10] D. Ackermann et G. Schmitz, « Detection and tracking of multiple microbubbles in ultrasound B-mode images », *IEEE Trans. Ultrason. Ferroelectr. Freq. Control*, vol. 63, nº 1, p. 72–82, 2015.

[11] Y. Desailly, O. Couture, M. Fink, et M. Tanter, « Sono-activated ultrasound localization microscopy », *Appl. Phys. Lett.*, vol. 103, nº 17, p. 174107, oct. 2013, doi: 10.1063/1.4826597.

[12] M. L. Ommen, M. Schou, C. Beers, J. A. Jensen, N. B. Larsen, et E. V. Thomsen, « 3D printed calibration micro-phantoms for super-resolution ultrasound imaging validation », *Ultrasonics*, vol. 114, p. 106353, 2021, doi: 10.1016/j.ultras.2021.106353.

[13] J. A. Jensen *et al.*, « Three-Dimensional Super-Resolution Imaging Using a Row–Column Array », *IEEE Trans. Ultrason. Ferroelectr. Freq. Control*, vol. 67, nº 3, p. 538-546, mars 2020, doi: 10.1109/TUFFC.2019.2948563.

[14] Y. Desailly, J. Pierre, O. Couture, et M. Tanter, « Resolution limits of ultrafast ultrasound localization microscopy », *Phys. Med. Biol.*, vol. 60, nº 22, p. 8723-8740, nov. 2015, doi: 10.1088/0031-9155/60/22/8723.

[15] V. Hingot, C. Errico, M. Tanter, et O. Couture, « Subwavelength motion-correction for ultrafast ultrasound localization microscopy », *Ultrasonics*, vol. 77, p. 17-21, 2017, doi: 10.1016/j.ultras.2017.01.008.

[16] J. Foiret, H. Zhang, T. Ilovitsh, L. Mahakian, S. Tam, et K. W. Ferrara, « Ultrasound localization microscopy to image and assess microvasculature in a rat kidney », *Sci. Rep.*, vol. 7, nº 1, p. 13662, déc. 2017, doi: 10.1038/s41598-017-13676-7.

[17] S. Harput *et al.*, « Two-Stage Motion Correction for Super-Resolution Ultrasound Imaging in Human Lower Limb », *IEEE Trans. Ultrason. Ferroelectr. Freq. Control*, vol. 65, nº 5, p. 803-814, 2018, doi: 10.1109/TUFFC.2018.2824846.

[18] V. Hingot, C. Errico, B. Heiles, L. Rahal, M. Tanter, et O. Couture, « Microvascular flow dictates the compromise between spatial resolution and acquisition time in Ultrasound Localization Microscopy », *Sci. Rep.*, vol. 9, nº 1, p. 2456, déc. 2019, doi: 10.1038/s41598-018-38349-x.

[19] S. Dencks, M. Piepenbrock, G. Schmitz, T. Opacic, et F. Kiessling, « Determination of adequate measurement times for super-resolution characterization of tumor vascularization », in *2017 IEEE International Ultrasonics Symposium (IUS)*, 2017, p. 1–4.

[20] B. Heiles *et al.*, « Ultrafast 3D Ultrasound Localization Microscopy Using a 32 $\times$ 32 Matrix Array », *IEEE Trans. Med. Imaging*, vol. 38, nº 9, p. 2005-2015, sept. 2019, doi: 10.1109/TMI.2018.2890358.

[21] O. M. Viessmann, R. J. Eckersley, K. Christensen-Jeffries, M. X. Tang, et C. Dunsby, « Acoustic super-resolution with ultrasound and microbubbles », *Phys. Med. Biol.*, vol. 58, nº 18, p. 6447-6458, sept. 2013, doi: 10.1088/0031-9155/58/18/6447.

[22] K. Christensen-Jeffries *et al.*, « Poisson Statistical Model of Ultrasound Super-Resolution Imaging Acquisition Time », *IEEE Trans. Ultrason. Ferroelectr. Freq. Control*, vol. 66, nº 7, p. 1246-1254, juill. 2019, doi: 10.1109/TUFFC.2019.2916603.

[23] H. Shroff, C. G. Galbraith, J. A. Galbraith, et E. Betzig, « Live-cell photoactivated localization microscopy of nanoscale adhesion dynamics », *Nat. Methods*, vol. 5, nº 5, Art. nº 5, mai 2008, doi: 10.1038/nmeth.1202.

[24] A. Oddone, I. V. Vilanova, J. Tam, et M. Lakadamyali, « Super-resolution imaging with stochastic single-molecule localization: Concepts, technical developments, and biological applications », *Microsc. Res. Tech.*, vol. 77, nº 7, p. 502-509, 2014, doi: https://doi.org/10.1002/jemt.22346.

[25] R. P. J. Nieuwenhuizen *et al.*, « Measuring image resolution in optical nanoscopy », *Nat. Methods*, vol. 10, nº 6, Art. nº 6, juin 2013, doi: 10.1038/nmeth.2448.

[26] N. Banterle, K. H. Bui, E. A. Lemke, et M. Beck, « Fourier ring correlation as a resolution criterion for super-resolution microscopy », *J. Struct. Biol.*, vol. 183, nº 3, p. 363-367, sept. 2013, doi: 10.1016/j.jsb.2013.05.004.

[27] M. van Heel et M. Schatz, « Fourier shell correlation threshold criteria », *J. Struct. Biol.*, vol. 151, nº 3, p. 250-262, sept. 2005, doi: 10.1016/j.jsb.2005.05.009.

[28] W. O. Saxton et W. Baumeister, « The correlation averaging of a regularly arranged bacterial cell envelope protein », *J. Microsc.*, vol. 127, nº 2, p. 127-138, 1982, doi: https://doi.org/10.1111/j.1365-2818.1982.tb00405.x.

[29] J. Brown *et al.*, « Investigation of Microbubble Detection Methods for Super-resolution Imaging of Microvasculature », p. 16.

[30] K. Christensen-Jeffries *et al.*, « Microbubble Axial Localization Errors in Ultrasound Super-Resolution Imaging », *IEEE Trans. Ultrason. Ferroelectr. Freq. Control*, vol. 64, nº 11, p. 1644-1654, nov. 2017, doi: 10.1109/TUFFC.2017.2741067.

[31] D. Espíndola, F. Lin, D. E. Soulioti, P. A. Dayton, et G. F. Pinton, « Adaptive multifocus beamforming for contrast-enhanced-super-resolution ultrasound imaging in deep tissue », *IEEE Trans. Ultrason. Ferroelectr. Freq. Control*, vol. 65, nº 12, p. 2255–2263, 2018.
[32] K. Diamantis, T. Anderson, M. B. Butler, C. A. Villagomez-Hoyos, J. A. Jensen, et V. Sboros, « Resolving Ultrasound Contrast Microbubbles Using Minimum Variance Beamforming », *IEEE Trans. Med. Imaging*, vol. 38, nº 1, p. 194-204, 2019, doi: 10.1109/TMI.2018.2859262.
[33] R. J. van Sloun, R. Cohen, et Y. C. Eldar, « Deep learning in ultrasound imaging », *ArXiv190702994 Cs Eess*, juill. 2019, Consulté le: oct. 03, 2019. [En ligne]. Disponible sur: http://arxiv.org/abs/1907.02994

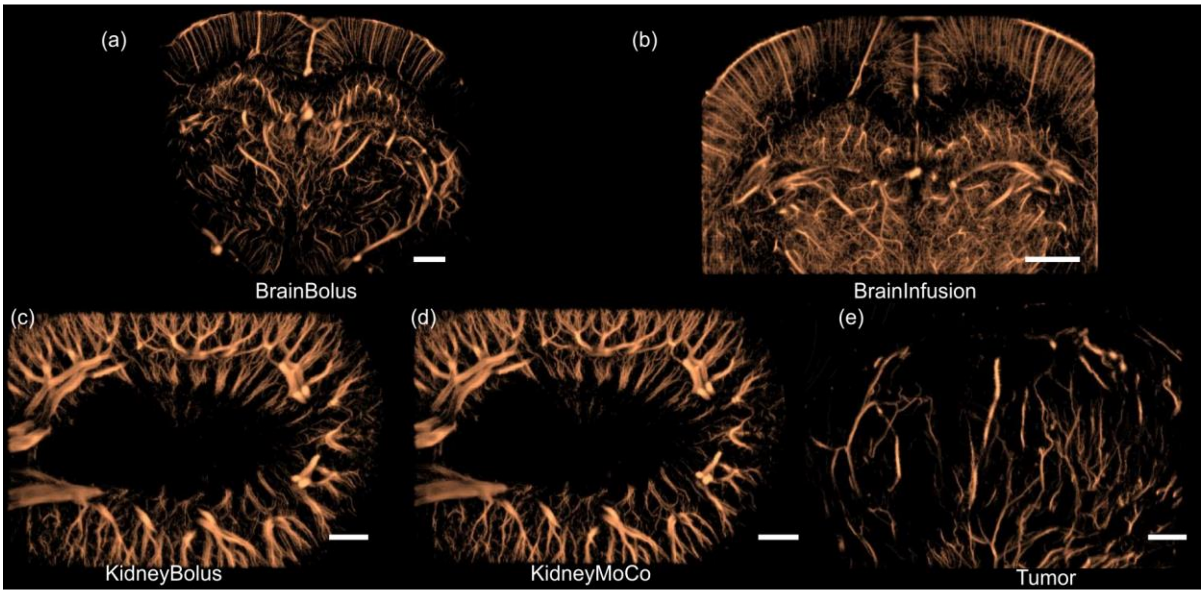

Figure 1 (a) ULM over the rat's brain with bolus of MB reconstructed from BrainBolus. (b) ULM over the rat's brain with infusion of MB reconstructed from BrainInfusion. (c) ULM over the rat's kidney with MB bolus injection reconstructed from KidneyBolus. (d) ULM over the rat's kidney with bolus injection and motion correction reconstructed from KidneyMoCo. (e) ULM over a mouse tumor with MB bolus injection reconstructed from Tumor. Scale bar 1 mm.

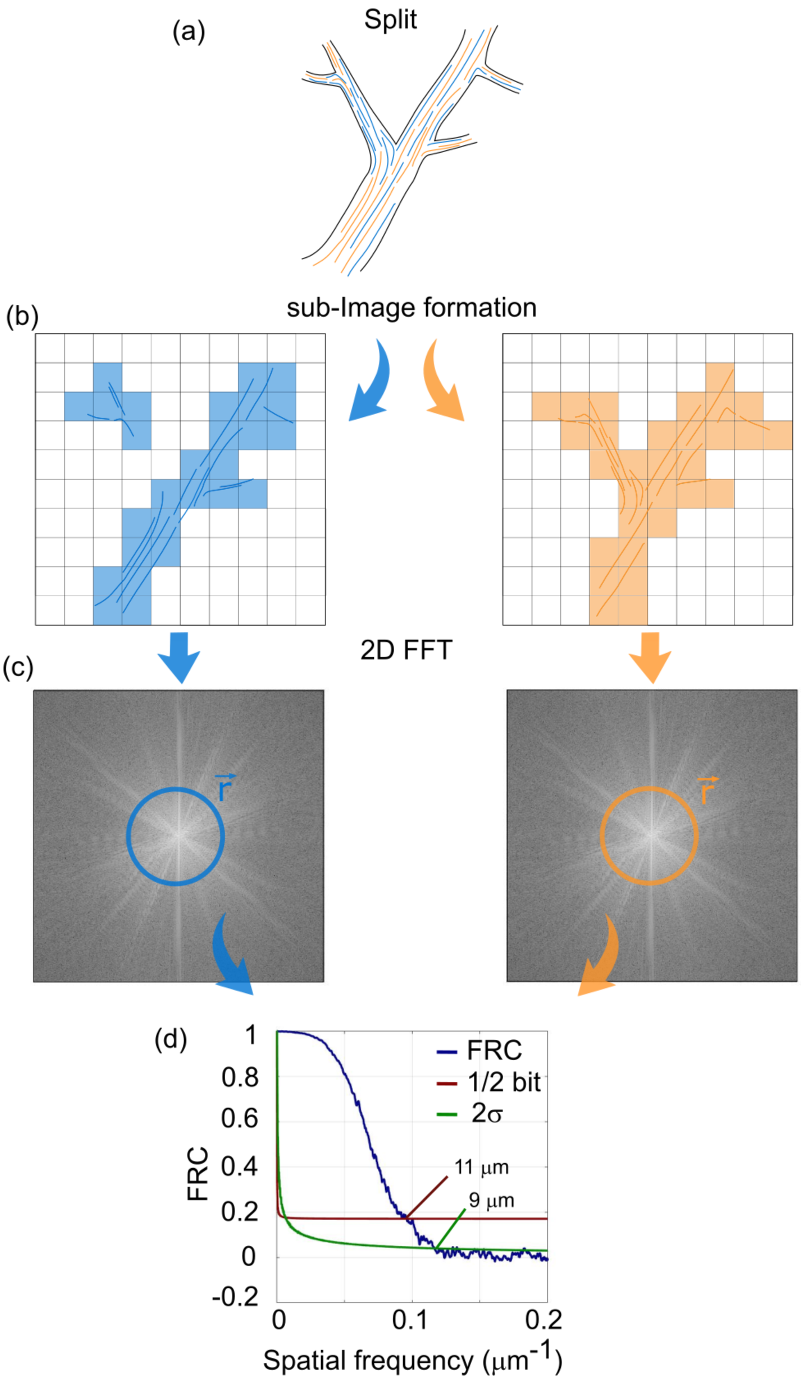

Figure 2: FRC calculation for ULM(a). Reconstruction of all MB tracks and separation in two equally filled subsets. (b) Reconstruction of the two corresponding sub-images. (c) Calculation of the two 2D Fourier spectrums. (d) Calculation of the FRC along iso-frequency rings and measure of resolution as the intersection with the 2-σ curve.

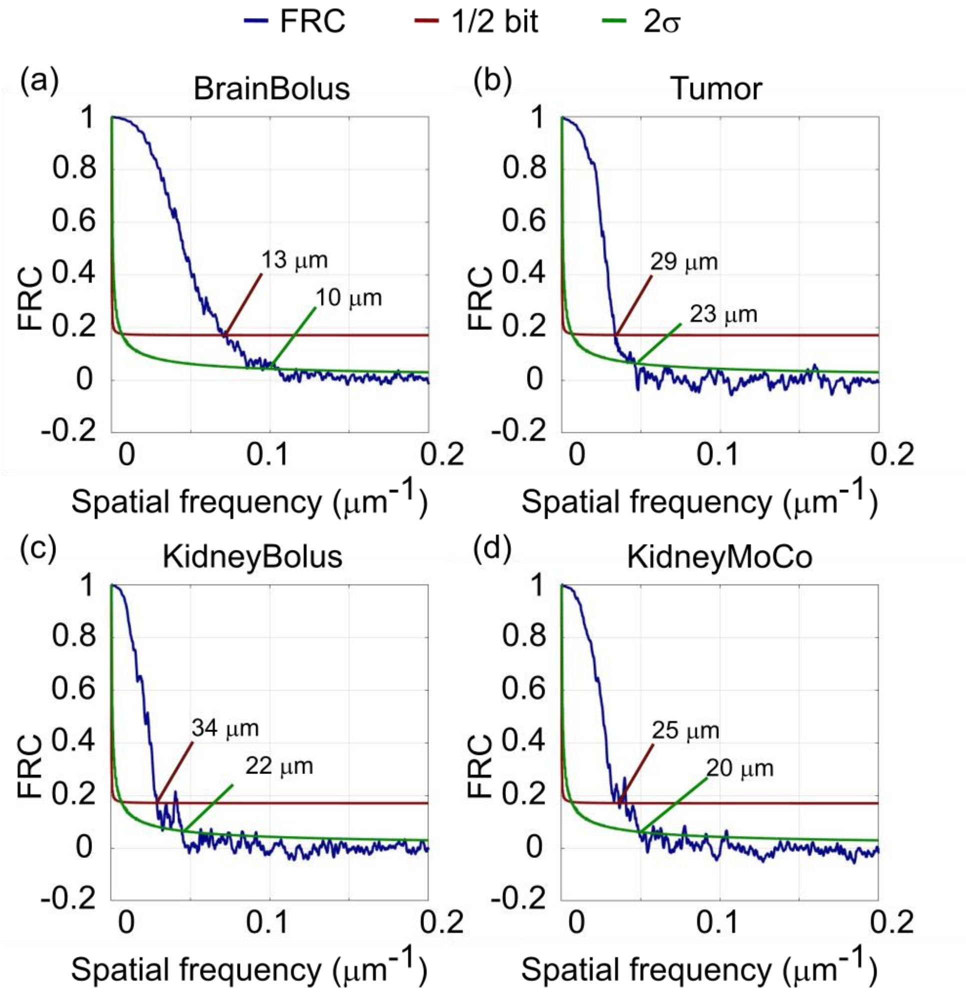

Figure 3: FRC curve with the 2-σ and the ½ bits threshold curves for the four datasets: (a) BrainBolus, (b) Tumor, (c) KidneyBolus, and (d) KidneyMoCo.

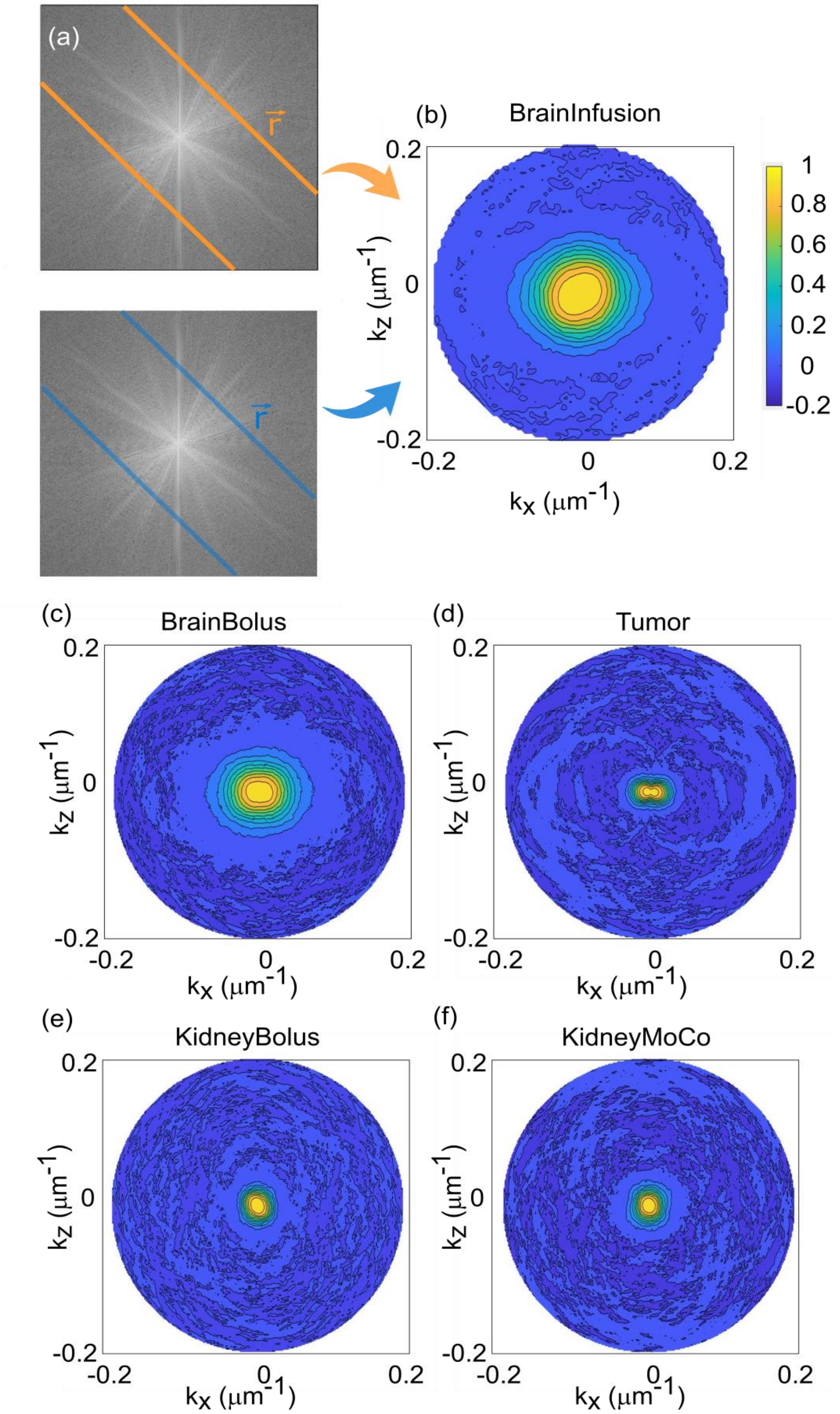

Figure 4: Adaption of the FRC for directional resolution estimation for the different datasets. (a) Principle of the Fourier Line Correlation calculation. (b) Corresponding FLC representation in BrainInfusion, (c) BrainBolus, (d) Tumor,(e) KidneyBolus, and (f) KidneyMoCo.

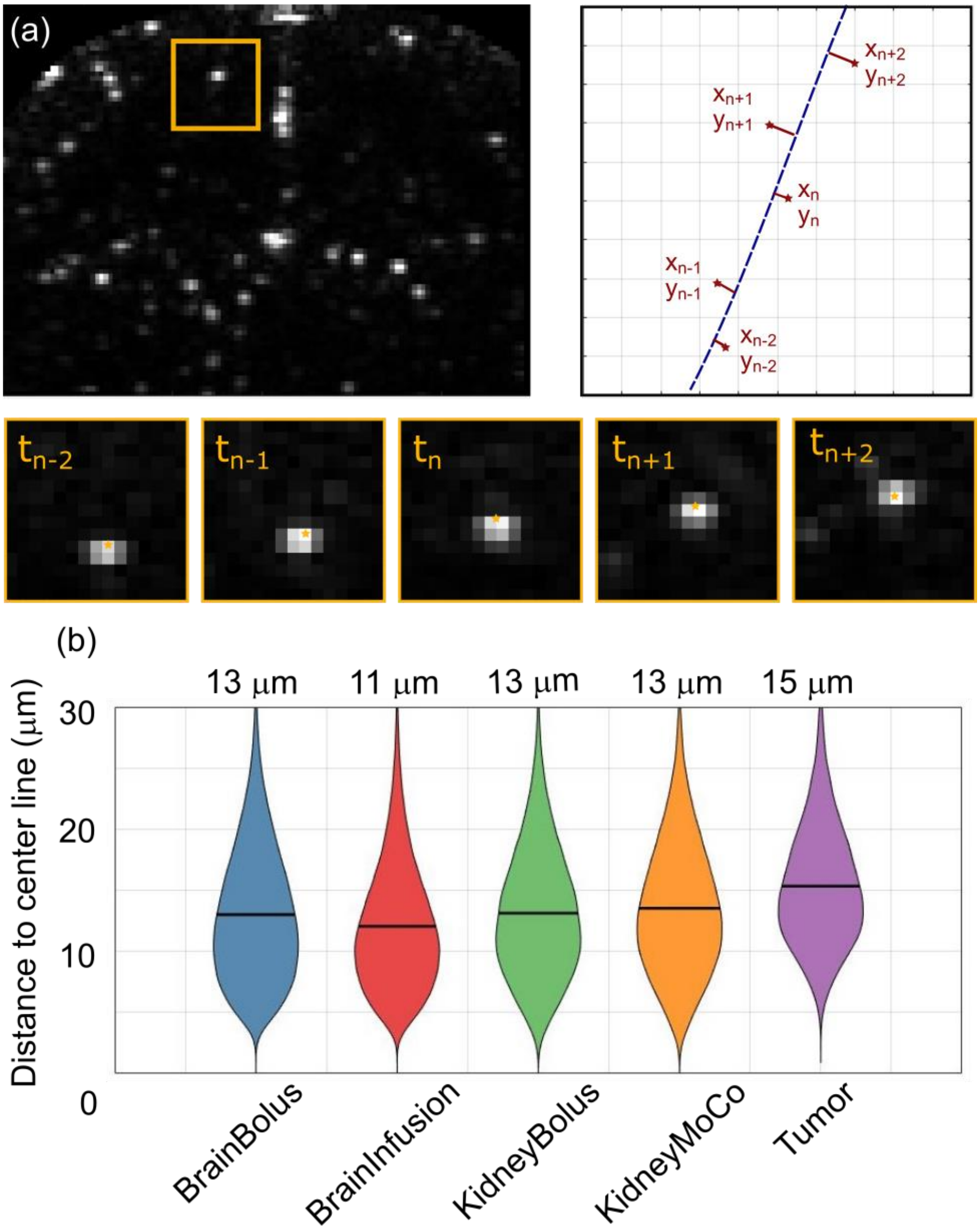

Figure 5: Estimation of the localization precision on in vivo data. (a) Principle of track-based localization estimation in BrainInfusion. (b) Localization precision estimated for all the datasets and represented as a violin plot with the corresponding mean written on top.

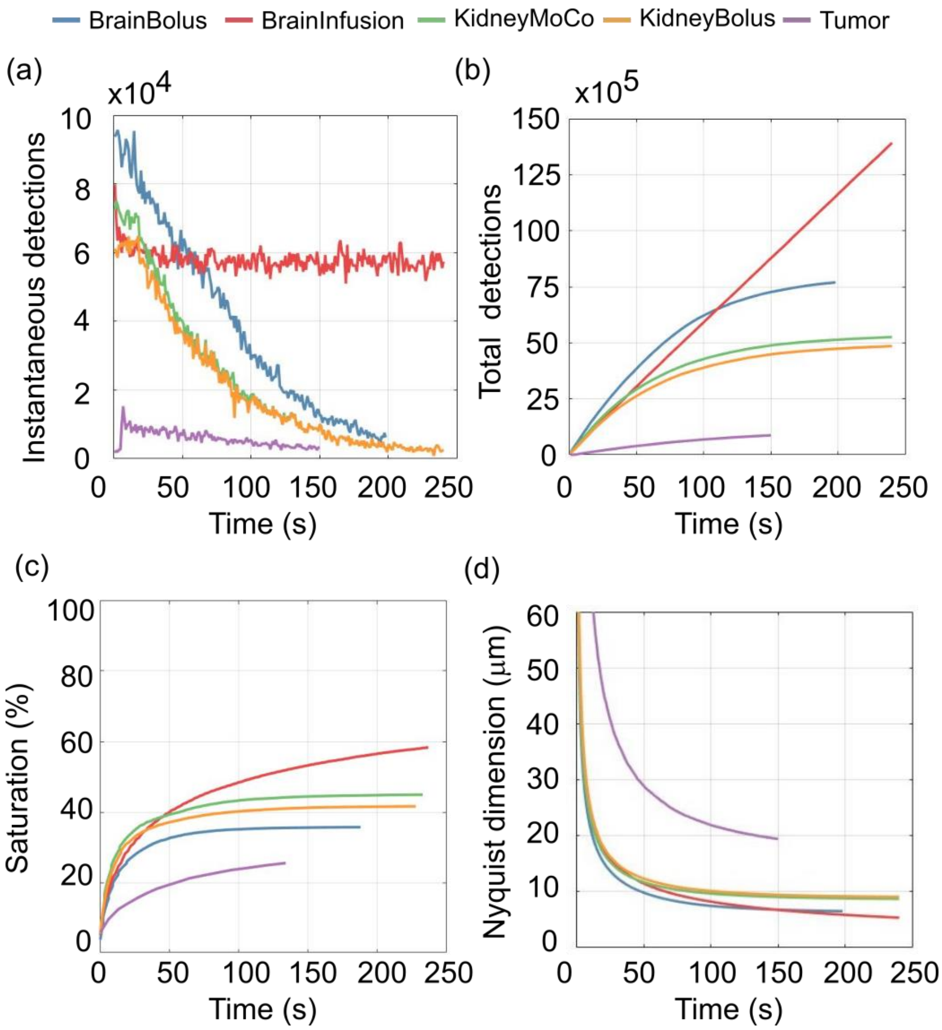

Figure 6: Temporal aspect of the different acquisitions in ULM. (a) Instantaneous MB count along time per bloc of 1s. (b) Cumulated MB count in time. (c) Saturation curves corresponding to the total area covered by MB detections on the image along time. (d) Corresponding Nyquist dimension calculated as in (1).

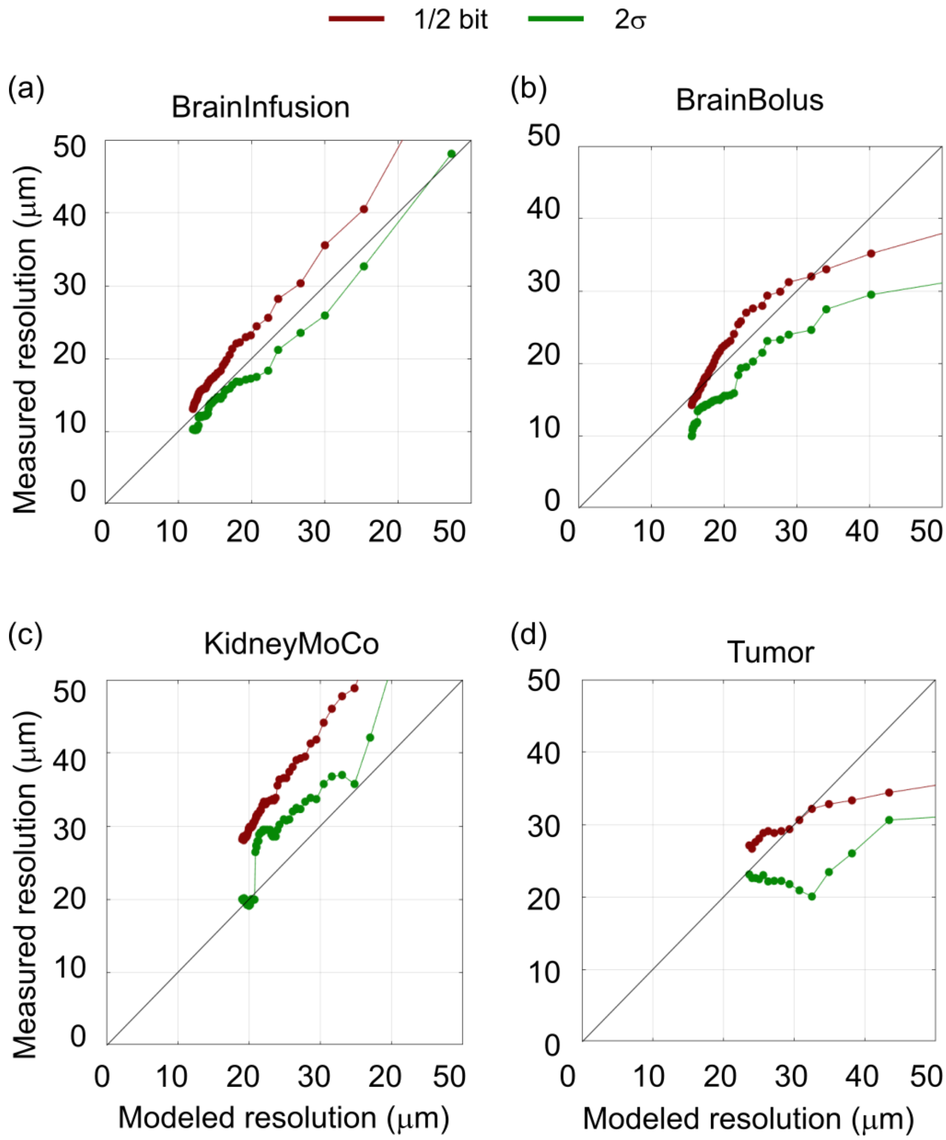

Figure 7: Relation between FRC measurement of resolution and the Nyquist dimension. (a) Theoretical representation of the resolution tradeoff with a curve following (2). (b) – (d), plotting of the FRC resolution for different acquisition times represented as a function of the corresponding Nyquist dimension in the different datasets. Points are separated by 2000 new detections.